High ^{3}He/^{4}He in central Panama reveals a distal connection to the Galápagos plume

David V. Bekaert[a,1], Esteban Gazel[b], Stephen Turner[c], Mark D. Behn[d], J. Marten de Moor[e], Sabin Zahirovic[f], Vlad C. Manea[g,h], Kaj Hoernle[i,j], Tobias P. Fischer[k], Alexander Hammerstrom[c], Alan M. Seltzer[a], Justin T. Kulongoski[l], Bina S. Patel[l], Matthew O. Schrenk[m], Sæmundur A. Halldórsson[n], Mayuko Nakagawa[o], Carlos J. Ramírez[p], John A. Krantz[a], Mustafa Yücel[q], Christopher J. Ballentine[r], Donato Giovannelli[a,m,s,t,u], Karen G. Lloyd[v], and Peter H. Barry[a]

[a]Marine Chemistry and Geochemistry Department, Woods Hole Oceanographic Institution, Woods Hole, MA 02543; [b]Earth and Atmospheric Sciences, Cornell University, Ithaca, NY 14853; [c]Department of Geosciences, University of Massachusetts, Amherst, MA 01003; [d]Department of Earth and Environmental Sciences, Boston College, Chestnut Hill, MA 02467; [e]Observatorio Vulcanológico y Sismológico de Costa Rica, Universidad Nacional, Heredia 86-3000, Costa Rica; [f]EarthByte Group, School of Geosciences, The University of Sydney, Sydney NSW 2006, Australia; [g]Computational Geodynamics Laboratory, Centro de Geociencias, Universidad Nacional Autónoma de México, Campus Juriquilla, Querétaro 76230, Mexico; [h]Faculty of Geology and Geophysics, University of Bucharest, Bucharest 010041, Romania; [i]Geosciences Research Division, GEOMAR Helmholtz Centre for Ocean Research Kiel, Kiel 24148, Germany; [j]Institute of Geosciences, Kiel University, Kiel 24118, Germany; [k]Department of Earth and Planetary Sciences, University of New Mexico, Albuquerque, NM 87131; [l]Scripps Institution of Oceanography, University of California San Diego, La Jolla, CA 92093; [m]Department of Earth and Environmental Sciences, Michigan State University, East Lansing, MI 48824; [n]NordVulk, Institute of Earth Sciences, University of Iceland, Reykjavík 101, Iceland; [o]Earth-Life Science Institute, Tokyo Institute for Technology, Tokyo 152-8550, Japan; [p]Research Department, Servicio Geológico Ambiental, Heredia 40301, Costa Rica; [q]Institute of Marine Sciences, Middle East Technical University, Erdemli 33731, Turkey; [r]Department of Earth Sciences, University of Oxford, Oxford OX1 4BH, United Kingdom; [s]Department of Biology, University of Naples Federico II, Naples 80138, Italy; [t]Institute for Marine Biological and Biotechnological Resources, National Research Council of Italy, Ancona 60125, Italy; [u]Department of Marine and Coastal Science, Rutgers University, New Brunswick, NJ 08854; and [v]Department of Microbiology, University of Tennessee, Knoxville, TN 37996

Edited by Donald W. Forsyth, Brown University, Providence, RI, and approved October 21, 2021 (received for review June 17, 2021)

It is well established that mantle plumes are the main conduits for upwelling geochemically enriched material from Earth's deep interior. The fashion and extent to which lateral flow processes at shallow depths may disperse enriched mantle material far (>1,000 km) from vertical plume conduits, however, remain poorly constrained. Here, we report He and C isotope data from 65 hydrothermal fluids from the southern Central America Margin (CAM) which reveal strikingly high ^{3}He/^{4}He (up to 8.9R_A) in low-temperature (≤50 °C) geothermal springs of central Panama that are not associated with active volcanism. Following radiogenic correction, these data imply a mantle source ^{3}He/^{4}He >10.3R_A (and potentially up to 26R_A, similar to Galápagos hotspot lavas) markedly greater than the upper mantle range (8 ± 1R_A). Lava geochemistry (Pb isotopes, Nb/U, and Ce/Pb) and geophysical constraints show that high ^{3}He/^{4}He values in central Panama are likely derived from the infiltration of a Galápagos plume–like mantle through a slab window that opened ∼8 Mya. Two potential transport mechanisms can explain the connection between the Galápagos plume and the slab window: 1) sublithospheric transport of Galápagos plume material channeled by lithosphere thinning along the Panama Fracture Zone or 2) active upwelling of Galápagos plume material blown by a "mantle wind" toward the CAM. We present a model of global mantle flow that supports the second mechanism, whereby most of the eastward transport of Galápagos plume material occurs in the shallow asthenosphere. These findings underscore the potential for lateral mantle flow to transport mantle geochemical heterogeneities thousands of kilometers away from plume conduits.

helium | mantle plume | slab window | mantle flow | geochemistry

The geochemical composition of the upper mantle is highly heterogeneous, even on a subkilometer scale (e.g., refs. 1 and 2). Plate tectonics controls the global chemical cycling between mantle and crustal reservoirs, with subduction being considered as the main driver for the reintroduction of incompatible element-rich components into the mantle (3, 4), especially into the source region of mantle plumes (5). Importantly, enriched magma sources are widespread in the upper mantle and sporadically observed both on- and off-axis at midocean ridges (see ref. 6 and the references therein). Although their origin was originally attributed to plume–ridge interactions (7) or small plumes randomly dispersed as small-scale heterogeneities in the mantle source of midocean ridge basalts (MORBs) (8), more recent studies, for instance, suggest fractionation during melting or metasomatic events (see refs. 3 and 6 and the references therein). More globally, "plume-like" geochemical signatures—also referred to as "geochemically enriched signatures" with respect to both trace elements and isotopic compositions—are observed in a wide range of geological settings including isolated seamounts (e.g., ref. 9), subduction zones (e.g., ref. 10), and intraplate continental regions (e.g., ref. 11).

Significance

We report the discovery of anomalously high ^{3}He/^{4}He in "cold" geothermal fluids of central Panama, far from any active volcanoes. Combined with independent constraints from lava geochemistry, mantle source geochemical anomalies in Central America require a Galápagos plume contribution that is not derived from hotspot track recycling. Instead, these signals likely originate from large-scale transport of Galápagos plume material at sublithospheric depths. Mantle flow modeling and geophysical observations further indicate these geochemical anomalies could result from a Galápagos plume-influenced asthenospheric "mantle wind" that is actively "blowing" through a slab window beneath central Panama. The lateral transport of plume material represents a potentially widespread yet underappreciated mechanism that scatters enriched geochemical signatures in mantle domains far from plumes.

Author contributions: E.G., D.G., K.G.L., and P.H.B. designed research; D.V.B., E.G., S.T., M.D.B., J.M.d.M., S.Z., V.C.M., K.H., T.P.F., A.H., A.M.S., J.T.K., B.S.P., M.O.S., S.A.H., M.N., C.J.R., J.A.K., M.Y., C.J.B., D.G., K.G.L., and P.H.B. performed research; D.V.B., E.G., S.T., M.D.B., J.M.d.M., S.Z., V.C.M., K.H., T.P.F., A.H., A.M.S., J.T.K., S.A.H., J.A.K., C.J.B., D.G., K.G.L., and P.H.B. analyzed data; and D.V.B. wrote a draft of the paper, with subsequent inputs from all coauthors.

The authors declare no competing interest.

This article is a PNAS Direct Submission.

[1]To whom correspondence may be addressed. Email: dbekaert@whoi.edu.

This article contains supporting information online at http://www.pnas.org/lookup/suppl/doi:10.1073/pnas.2110997118/-/DCSupplemental.

Published November 19, 2021.

The extent and distribution of certain mantle geochemical heterogeneities are complicated by a large number of competing processes taking place throughout Earth history. However, coherent mantle geochemical anomalies have been related to patterns of mantle flow (7), thereby providing insights into mantle geodynamics. The buoyancy-driven lateral transport of plume material by local pressure gradients at sublithospheric depths has previously been described (12–14). While this process may explain local transport of plume material, its lateral extent is too limited to account for the large-scale dispersal of plume material across the upper mantle. Additional studies have suggested the potential for "distal plume–ridge interactions" and far-field influence of plumes beyond the classically considered length scale of a plume's lateral spreading radius (15, 16). Because buoyant plumes tend to flow toward regions where the lithosphere is thinner, variations in lithospheric thickness along rifting and seafloor spreading axes could potentially channelize the lateral flow of mantle plume material and act as a conduit for its lateral transport over long distances (i.e., >1,000 km) (12, 17). However, the global frequency and extent of lateral plume material movement at sublithospheric depths remain poorly understood because of inherent difficulties associated with the observation and quantification of the underlying processes.

In the southern segment of the Central America Margin (CAM), geographically restricted lavas with plume-like geochemical signatures formed over the last ~5 My (10). Their origin remains actively debated, potentially reflecting magma source heterogeneities associated with the recycling of subducted Galápagos hotspot track material (*SI Appendix*, Fig. S1), direct contribution from a mantle plume source, or a combination of both (10, 18–21). The absence of a Wadati–Benioff zone associated with subduction from southeastern Costa Rica through Panama has been interpreted to reflect the presence of a slab window (22), potentially allowing the influx of hot asthenosphere beneath Central America (10, 18). Although the absence of a subducting slab as a fluid reservoir is a reasonable explanation for the lack of active arc volcanism in the region (23), the potential connection between the absence of deep seismicity and the emergence of plume geochemical signatures in the arc remains enigmatic. To identify the sources of volcanism in the southern CAM, helium and carbon isotopes were measured in deeply sourced hydrothermal fluid (n = 43) and gas (n = 22) samples collected in Costa Rica and Panama between 2005 and 2018. These results are combined with lava geochemistry systematics in the CAM, for which we present 1) $^{206}Pb/^{204}Pb$, Ce/Pb, and Nb/U data for lavas collected at La Providencia in the back-arc region of the CAM and 2) an updated compilation of literature data for the entire CAM. Taken together with independent constraints from geophysics and a global mantle flow model (24), these geochemical data support lateral transport of enriched plume material at sublithospheric depths from the Galápagos plume to the CAM.

Results

Helium Isotope Systematics. Despite the general geochemical heterogeneity of the upper mantle (7, 8), the $^3He/^4He$ of MORBs is remarkably uniform [R/R_A = 8 ± 1 (25), in which R = $^3He/^4He_{sample}$ and R_A = $^3He/^4He_{air}$] compared to plume-sourced volcanism (R/R_A in the range ~4 to 40) (25). At subduction zones, gases discharged from arc volcanoes have He isotope compositions intermediate between the convecting upper mantle sampled by MORBs and continental crust [R/R_A = ~0.01 (25)], with a global mean of 5.4 ± 1.9 R_A (26, 27). Here, He isotope data from hydrothermal waters, collected over 15 y and analyzed in three different laboratories (*SI Appendix*), reveal an along-arc (southeastward) increase from 1 to 7 R_A in Costa Rica and up to ~9 R_A in Panama (Fig. 1). The highest $^3He/^4He$ of 8.86 ± 0.44 R_A was measured in a "cold" (50 °C) spring in the volcanically dormant region of central Panama, which is a unique and puzzling discovery. Notably, very few similarly high $^3He/^4He$ values have been reported in samples from other arc segments, and they all come from 1) ≥100 °C summit volcanic fumaroles from the Lesser Antilles, Papua New Guinea, and Java (26, 28–30) or 2) ≥300 °C crater fumaroles of Galeras volcano (Colombia) during a brief high-$^3He/^4He$ event preceding the 1992 explosive eruption [8.84 ± 0.63Ra (31); *SI Appendix*, Fig. S3]. In both cases, they are interpreted to reflect pure upper mantle He signatures with no or limited crustal He contribution. The 8.86 ± 0.44 R_A measurement from central Panama is exceptional, as it is the highest value ever measured in a geothermal spring far from an active volcano.

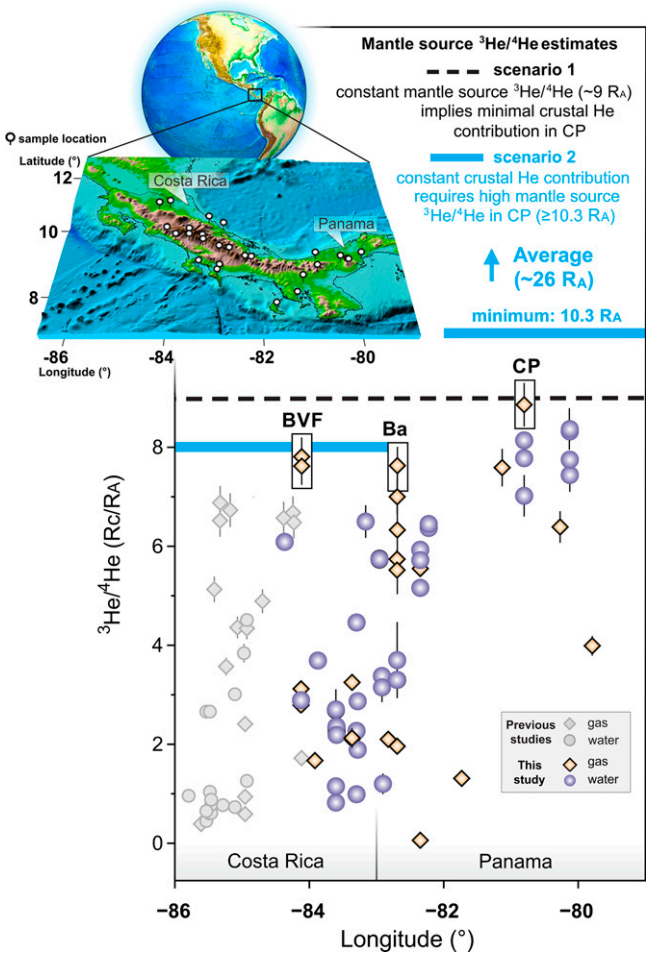

Fig. 1. Longitudinal evolution of geothermal fluid (circles) and gas (diamonds) $^3He/^4He$ in the southern CAM and estimation of the mantle source $^3He/^4He$ beneath central Panama. Previous data from P.H. Barry et al. (27) are reported in gray. BVF: Behind the Volcanic Front, in Costa Rica. Ba: Barú volcano in Panama. CP: central Panama. (*Inset*) General location of our study area. Mantle source $^3He/^4He$ estimates for scenarios one and two correspond to cases of 1) magma upwelling from the upper mantle with no crustal contribution and 2) mixing between crustal He and a high $^3He/^4He$ mantle source, respectively. We favor the second scenario which implies a mantle source $^3He/^4He \geq 10.3$ R_A and potentially up to ~26 R_A in central Panama (see last paragraph of the section *Insights from Lava Geochemistry in the CAM* and *SI Appendix*, Figs. S5–S7).

Carbon Isotope Systematics. Similar to He, CO_2 emitted in subduction zones typically represents a mixture between mantle and crustal components (32). Here, the covariations of $\delta^{13}C$

versus Vienna Pee Dee Belemnite of inorganic C (noted $\delta^{13}CO_2$) and $CO_2/^3He$ for fluid and gas samples (*SI Appendix*, Figs. S9 and S10) require mixing between deep mantle fluids and slab-derived components followed by isotope fractionation associated with calcite precipitation at temperatures ranging from 25 to 125 °C (*SI Appendix*, Fig. S9). Data from the 2018 field campaign also show increasingly negative $\delta^{13}C$ with decreasing dissolved inorganic carbon (DIC) content following steep Rayleigh fractionation curves at low $\delta^{13}C$ values (*SI Appendix*, Fig. S10). These data follow predictions for calcite precipitation at ∼65 °C, starting from a $\delta^{13}C$ of +2‰ and an initial DIC of 60 mmol/L^{-1} (*SI Appendix*, Fig. S10). We estimate that >75% of the DIC within the fluids with high DIC ∼60 mmol.l^{-1} originates from the mantle wedge rather than in situ carbonate dissolution (*SI Appendix*). The positive $\delta^{13}C$ for the starting composition of DIC, significantly higher than the range of $\delta^{13}C$ for gas samples (–5 to –1 ‰, *SI Appendix*, Fig. S9), is interpreted to reflect equilibrium isotopic fractionation [∼+7‰ (33)] during partial dissolution of pure mantle CO_2 gas [–5‰ (32)] into aqueous fluids (27). Overall, these data support the recent finding (27) that calcite precipitation within the crust is a significant sink of C in subduction zones. When reported against longitude, $\delta^{13}C$ of DIC suggests a progressive increase from low values in the west (Costa Rica)—indicative of extensive C sequestration because of calcite precipitation—toward positive $\delta^{13}C$ (∼+2‰) and high DIC in the east (central Panama), approaching the mantle wedge value (*SI Appendix*, Fig. S10).

Discussion

Origin of High $^3He/^4He$ in Central Panama. The elevated $^3He/^4He$ observed in central Panama requires that either 1) the fluids are derived directly from upwelling magma without incorporation of any crustal He (scenario one) or 2) He in the fluids represents a mixture of crustal He and a mantle source with higher $^3He/^4He$ than that of the convecting upper mantle (scenario two). In volcanic settings, $^3He/^4He$ of hydrothermal fluids are typically observed to be highest close to eruptive vents and rapidly decrease toward radiogenic values ($^3He/^4He < 1$ R_A) away from volcanic centers because of reduced mantle input and enhanced contribution from the underlying crust (26, 27, 34). The highest $^3He/^4He$ values measured in crater fumaroles (>70 °C) along the CAM are from the Turrialba (8.1 R_A), Poás (7.6 R_A), and Irazú (7.2 R_A) volcanoes in Costa Rica and the Mombacho volcano (7.6 R_A) in Nicaragua (35–37), all markedly lower than the 8.9 R_A value reported here from cold springs in central Panama. Assuming a homogeneous upper mantle source with $^3He/^4He$ of 9 R_A across the southern CAM, scenario one suggests a very low crustal He contribution in the geothermal fluids of central Panama (≤1%), lower than that of high-temperature fumaroles (>10%) (*SI Appendix*, Fig. S5). This scenario seems highly unlikely, given that the high $^3He/^4He$ cold springs are hundreds of kilometers away from currently active volcanic centers. This interpretation is supported by 1) the absence of active volcanism in central Panama during the Holocene (38) and 2) the roughly constant continental crust thickness (∼35 km) across the southern CAM (*SI Appendix*, Fig. S4), implying that significant crustal He contributions, as observed in the cold geothermal fluids of Costa Rica (27, 35), should also be widespread in central Panama. While the suggestion that the high $^3He/^4He$ values in central Panama instead reflect the existence of a ^3He-rich mantle source beneath the region (scenario two) may be equally remarkable, this scenario is supported by observations of lava geochemistry and geodynamic constraints.

Insights from Lava Geochemistry in the CAM. To elucidate the origin of the high $^3He/^4He$ in the southern CAM, we compare geochemical systematics of typical arc lavas from El Salvador, Honduras, and Nicaragua to the volumetrically minor lavas that have formed over the last 5 My in regions where the highest $^3He/^4He$ values are observed (Fig. 1), namely 1) in central Panama, 2) near the adakitic Barú volcano, and 3) alkaline basaltic volcanism behind the volcanic front (BVF) in Costa Rica (10, 18, 21, 39, 40) (*SI Appendix*, Fig. S1*C*). While the adakites are generally considered to reflect the recycling of Galápagos hotspot track material from the subducting slab, the origins of the alkaline geochemical signatures are less clear (10, 20, 21). To disentangle mantle- versus slab-derived plume signatures, Pb isotopes ($^{206}Pb/^{204}Pb$) were combined with Nb/U and Ce/Pb data across the CAM (Fig. 2). Pb isotopes are particularly useful because the signatures of the different Galápagos domains are distinct from MORBs (41–43). Ce/Pb systematics, on the other hand, discriminate between mantle- and slab-derived components, with oceanic mantle sources being characterized by high and relatively constant Ce/Pb [≥20 (44)], whereas subduction-related magmas show distinctly lower Ce/Pb because of the low Ce/Pb of sediments and the preferential addition of Pb relative to Ce by slab-derived fluids and hydrous melts (45, 46). Combining $^{206}Pb/^{204}Pb$ and Ce/Pb systematics can therefore indicate if Galápagos plume material has infiltrated the subarc mantle and identify the source (mantle versus slab) of this component.

Arc-front lavas from El Salvador to Nicaragua and BVF lavas from Honduras demonstrate mixing between typical MORB-like mantle ($^{206}Pb/^{204}Pb$∼18.8) and slab ($^{206}Pb/^{204}Pb$∼18.5) components that are unrelated to the Galápagos plume (Fig. 2*A*). Notably, adakites and alkaline lavas in central Panama and BVF in Costa Rica (19, 47) span a similar range of Ce/Pb values from the low slab-controlled range (i.e., adakites) up to the pure oceanic mantle values (alkaline basalts). However, the adakites and alkaline lavas maintain Galápagos-like $^{206}Pb/^{204}Pb$ values at both high and low Ce/Pb values (Fig. 2*A*). Whereas the high $^{206}Pb/^{204}Pb$ signals associated with low Ce/Pb values likely reflect recycling of subducted hotspot track material, the alkaline lavas with high Ce/Pb and Galápagos-like $^{206}Pb/^{204}Pb$ must derive from Galápagos-type plume material not associated with hotspot track recycling. This indicates that plume-like signatures in the CAM cannot be solely accounted for by the recycling of slab-derived hotspot track material but require an influx of mantle material carrying a high $^{206}Pb/^{204}Pb$ signature similar to Galápagos Central Domain lavas. The existence of distinct mixing trends in Ce/Pb versus Nb/U space supports this interpretation (Fig. 2*B*), requiring contribution from a slab component and two distinct mantle domains (MORB-like and Galápagos-like). Notably, $^{206}Pb/^{204}Pb$–Ce/Pb–Nb/U data from La Providencia lavas, which exhibit no evidence of slab influence, confirm that the typical mantle behind the arc (prior to the infiltration of slab material) resembles the MORB mantle (Fig. 2) as observed for back-arc lavas from Honduras (Utila and Yohoa). The diminishing Galápagos mantle signature in back-arc lavas going from Costa Rica to Nicaragua to La Providencia therefore indicates that the influx of Galápagos-like $^{206}Pb/^{204}Pb$ mantle recorded in alkaline lavas does not originate from the Caribbean basin and must instead be connected with the Galápagos plume.

The most straightforward explanation for the sudden emergence (∼5 Mya) of enriched lavas in the CAM back arc is that a slab window opened ∼8 Mya (18, 22), allowing hot asthenosphere to flow into the mantle wedge beneath the back arc (10). The location of adakites (near the Barú volcano) (Fig. 2) spatially coincides with the purported edge of the slab window, suggesting that their strong slab signature (i.e., low Ce/Pb and Nb/U, Fig. 2*A*) represents melting of the slab edge during the influx of hot asthenosphere. The Galápagos Central Domain, which matches the $^{206}Pb/^{204}Pb$ composition of enriched lavas in the CAM (43), reflects the primitive plume composition with

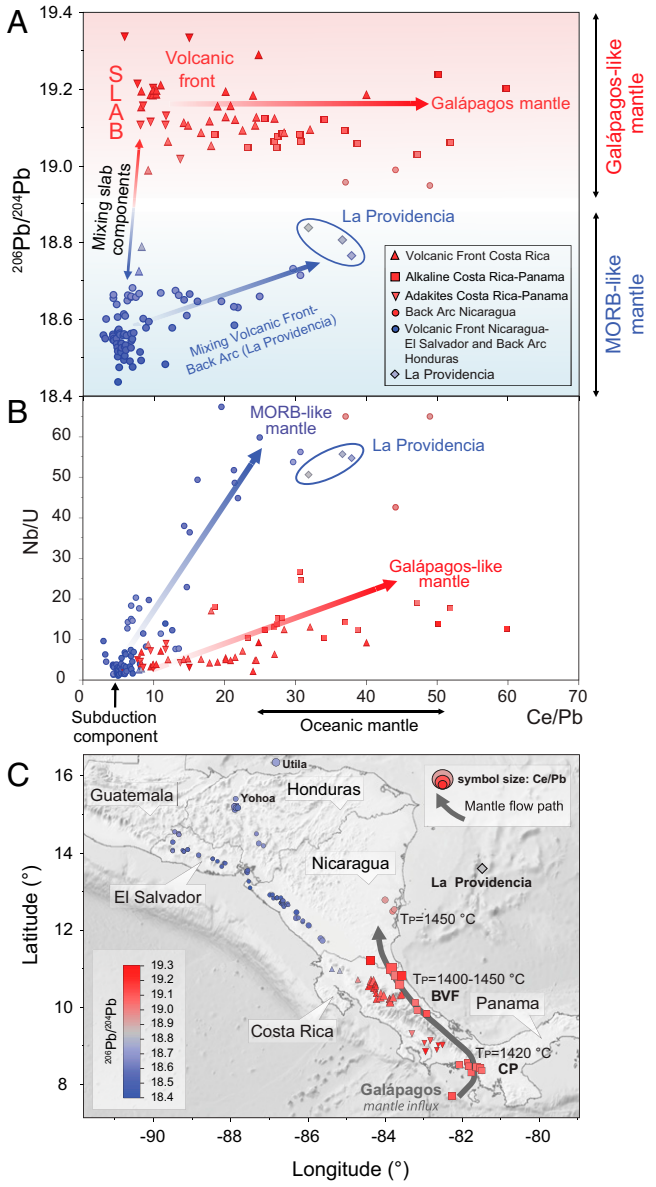

Fig. 2. $^{206}Pb/^{204}Pb$–Nb/U–Ce/Pb systematics in the CAM. $^{206}Pb/^{204}Pb$–Ce/Pb (*A*) and Nb/U–Ce/Pb (*B*) diagrams showing that alkaline lavas in central Panama (CP) and BVF in Costa Rica contain Galápagos geochemical signatures (high $^{206}Pb/^{204}Pb$) inherited from both a slab component (low Nb/U and Ce/Pb) and an oceanic mantle source end member (high Nb/U and Ce/Pb). High Ce/Pb in alkaline magmas show direct evidence for a Galápagos-like mantle component in their Pb isotopes (21, 47), whereas adakites have low Ce/Pb indicative of strong slab contributions. (*C*) Map of the CAM representing lava sample locations with symbol size and color referring to Ce/Pb and $^{206}Pb/^{204}Pb$, respectively. Symbol shapes correspond to sample localities detailed in the legend of *A*. The gray arrow materializes the purported direction of the mantle influx from the Galápagos plume oceanic domain (Fig. 3). Manifestations of this Galápagos mantle component (CP and BVF) spatially coincide with high mantle potential temperatures (T_P, up to 1,450 °C versus ~1,350 °C in the upper mantle) (10) as well as high $^{3}He/^{4}He$ in hydrothermal fluids and gas (Fig. 1), suggesting that all of these features are consistent with a Galápagos mantle component.

$^{3}He/^{4}He$ up to 30 R_A (48). The high $^{3}He/^{4}He$ detected in geothermal fluids <70 °C BVF in Costa Rica and central Panama (Fig. 1) are thus most consistent with an influx of Galápagos mantle (scenario two). A compilation of He isotope data for all geothermal fluids <70 °C reported to date in Costa Rica (*SI Appendix*) shows only one location (BVF) that exhibits $^{3}He/^{4}He$ >7 R_A (up to 7.8 R_A; Fig. 1). All the other geothermal fluids <70 °C from Costa Rica (n = 68) have an average $^{3}He/^{4}He$ of 2.77 ± 1.88 R_A, with a maximum value of 6.88 R_A within 8 km of the Rincón de la Vieja volcano (27). In the first paragraph in the *Discussion* section, we argued that the ~9 R_A values in central Panama are unlikely to represent direct sampling of an upper mantle source given that the $^{3}He/^{4}He$ of the high-temperature crater fumaroles require some mixing with crustal He. Using a similar logic, we can estimate the range of $^{3}He/^{4}He$ that is likely to represent the mantle source beneath central Panama ($^{3}He/^{4}He_{CP}$). For example, considering that the mantle beneath Costa Rica ($^{3}He/^{4}He_{CR}$) has a $^{3}He/^{4}He \geq 8$ R_A, the maximum (6.88 R_A) and average (2.77 R_A) $^{3}He/^{4}He$ values in geothermal fluids <70 °C require crustal He contributions of >14 and >66%, respectively (*SI Appendix*, Figs. S6 and S7). If crustal He contributions are similar in Costa Rica and central Panama (which would be consistent with the roughly constant crustal thickness across the CAM, scenario two; *SI Appendix*, Fig. S4), then the $^{3}He/^{4}He_{CP}$ must be ≥10.3 R_A (assuming 14% crustal He) and potentially up to ~26 R_A (assuming 66% crustal He), similar to the Galápagos Central Domain (48) (Fig. 1 and *SI Appendix*, Figs. S6 and S7). Our result that $^{3}He/^{4}He_{CP} \geq {}^{3}He/^{4}He_{CR}+2.3R_A$ is satisfied throughout the entire range of plausible $^{3}He/^{4}He_{CR}$ values (*SI Appendix*, Fig. S7), further supporting the existence of a ^{3}He-rich mantle source beneath central Panama. Importantly, a slab-derived origin of the high $^{3}He/^{4}He$ in the CAM is highly implausible because, 1) unlike other elements, He is lost from the slab to the surface during the earliest stages of subduction, and it does not accumulate or laterally migrate beneath the arc, and 2) no known hotspot track component subducts directly beneath central Panama (see plate tectonic reconstruction, Movie S1). As such, we argue that the ^{3}He-rich mantle source beneath central Panama likely represents direct evidence for the influx of Galápagos mantle through the Panama slab window (49).

Origin of the Plume-Like Oceanic Mantle Component in the CAM. Geochemical constraints (e.g., high Ce/Pb and $^{206}Pb/^{204}Pb$ values; Fig. 2) require the presence of Galápagos plume–like material that is not derived from hotspot track recycling in the mantle source of the CAM. In principle, this observation could arise from "random" geochemical heterogeneities dispersed throughout the upper mantle (1). However, this scenario would not explain the northwest migration in the back-arc alkaline lavas and observed increase in mantle potential temperature (10) or the systematic Galápagos plume signature associated with high Ce/Pb lavas of the CAM (Fig. 2).

An alternative explanation for the occurrence of Galápagos plume–like material in the mantle source of the CAM volcanism is lateral transport of geochemically enriched material from the Galápagos plume. The age (and thus the thickness) of the oceanic lithosphere increases toward the CAM (see plate tectonic reconstruction, Movie S1). To overcome the thickening of the lithosphere and transport plume material over such long distances (~1,400 km) requires a combination of sufficiently large plume buoyancy and efficient channeling of the plume material flow at the base of the lithosphere (50). The Panama Fracture Zone (PFZ), which represents the transform plate boundary between the Cocos and the Nazca plates and connects the Galápagos plume domain to the CAM (*SI Appendix*, Fig. S1 and Fig. 3), could constitute a zone of thinned lithosphere that acts as a channel for the lateral flow of Galápagos plume material. This scenario is in line with significant plume–ridge interaction in the Galápagos region (43, 51) at sublithospheric to asthenospheric depths (52), potentially requiring high melt fractions (as opposed to solid-state mantle

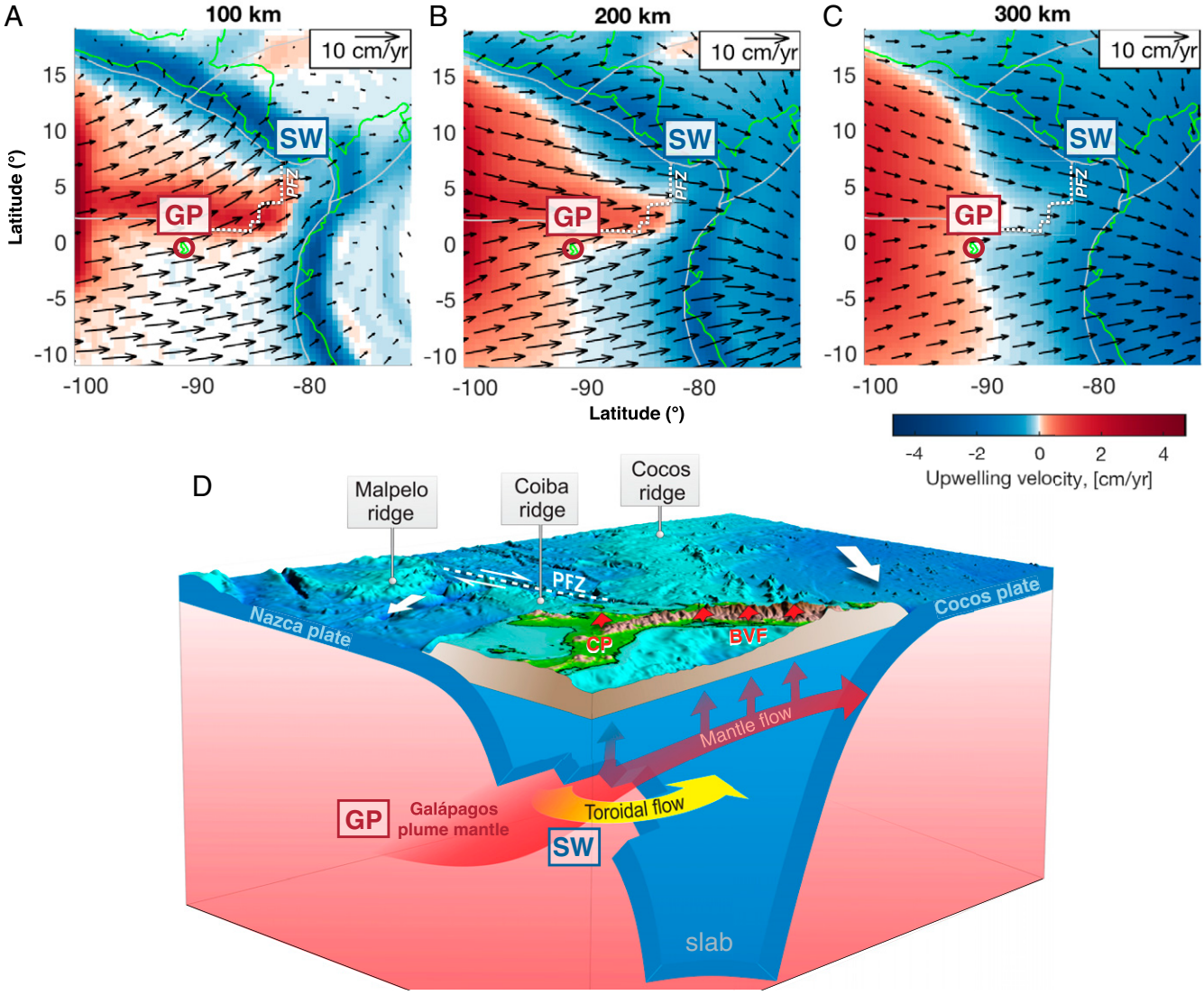

Fig. 3. A 1,400 km-long upwelling mantle flow connects the Galápagos plume to the Panama slab window. Asthenospheric mantle flow of the eastern Pacific mantle as predicted from global viscous flow modeling (24). Slices through the upper mantle shown at depths of 100 km (*A*), 200 km (*B*), and 300 km (*C*). Contours of emerged lands are reported in green with the Galápagos islands being denoted by a red circle (*A*–*C*). Black arrows depict horizontal velocity vectors. Colors show vertical components of mantle flow velocity with blue and red corresponding to downwelling and upwelling flow, respectively. *D* shows a three-dimensional representation of the mantle flow connecting the oceanic domain around the Galápagos plume and the central Panama slab window. Once the "plume" material flows through the slab window, the direction of mantle flow would deviate northward because of the toroidal flow field around the edge of the slab (60). The arc-parallel mantle flow then moves up and spreads out in the direction of thinner lithosphere to the bottom of the overriding plate away from the Talamanca Mountain (positive topography shown in brown color) root. This influx of Galápagos plume–enriched asthenosphere accounts for the observation of mantle plume geochemical signatures (e.g., high $^{3}He/^{4}He$) in the volcanically dormant region of central Panama and BVF in Costa Rica. CP: Central Panama. BVF: Behind the Volcanic front. GP: Galápagos Plume mantle. SW: Slab Window. PFZ: Panama Fracture Zone.

flow) for the plume material channeling to be sustained over >1,000 km (17) toward the CAM.

The lateral transport of plume material can also be facilitated by large-scale mantle flow. To test this mechanism, we use a global mantle flow model (24) that combines flow driven by relative plate motions, mantle density structures, and westward lithosphere rotation. While this flow model does not take the existence of a slab window under central Panama into account, it does include the effects of a stiff oceanic lithosphere that thickens with age. These simulations show a clear eastward-upwelling "mantle wind" in the shallow asthenosphere that connects the oceanic domain around the Galápagos plume to the southern CAM (Fig. 3 *A* and *B*). At greater depths, where the influence of plate motion becomes less prominent, the upwelling and lateral flow velocities decrease, and the general direction of flow progressively deviates toward Colombia (Fig. 3 *B* and *C*). Overall, our model is consistent with eastward dispersal of Galápagos plume material at depth, which could help explain the surprising lack of high $^{3}He/^{4}He$ along the Galápagos spreading center (53). Age dating further shows that young (<2 My old) volcanism with Galápagos Central Domain-type composition occurs along the Cocos Ridge to within 300 km of Costa Rica and volcanism as young as 5 My old exists on the Coiba Ridge offshore of western Panama, consistent with the presence of plume material in the upper mantle beneath the hotspot tracks (54, 55). The sense of shear predicted by our

simulations also agrees with teleseismic observations of shear-wave splitting in southern Costa Rica (56), which bolsters the scenario of a Pacific to Caribbean mantle flow.

The prediction that Galápagos plume material is being transported in the upper asthenosphere toward central Panama (from global mantle flow field simulations) provides a straightforward explanation for the Galápagos plume–like mantle component detected in the CAM. Specifically, the decompression of Galápagos plume mantle as it flows through the central Panama slab window would promote melting and the emplacement of magma [as witnessed over the last 5 My; Fig. 2 (10, 18, 21)], effectively releasing Galápagos plume–derived He under central Panama. This upwelling mantle He component then interacts with the ∼35-km thick continental crust, where it gets diluted with crustal He to produce the He isotope signatures observed in surface fluids of the CAM (Fig. 1). It is noteworthy that the anomalously high values of DIC measured in central Panama could be explained by substantial contributions from mantle-derived and recycled components. However, a significant contribution from sediments is unlikely, as these are characterized by largely negative $\delta^{13}C$, around –30‰, which is much lighter than the $\delta^{13}CO_2$ values measured here for gas samples (in the range −5 to 0‰; *SI Appendix*, Fig. S9). A bimodal origin of carbon from both the mantle and recycled carbonates is in agreement with Pb isotope–Ce/Pb-Nb/U systematics (Fig. 2) pointing to the existence of both recycled and primitive components in the source of adakites and alkaline basalts in the southern CAM.

Implications. From Mexico to Patagonia, subducting oceanic lithosphere and thick continental keels in the overriding plate form a nearly continuous barrier impeding the flow of the upper mantle. The formation of a slab window in the eastern Pacific (18, 22) is consistent with the large-scale view of mantle dynamics, whereby material from the shrinking Pacific basin is transferred to the growing mantle reservoir beneath the opening Atlantic basin through the subducting Cocos–Nazca Plates (57). Interestingly, plate tectonic reconstruction models (Movie S1) indicate that the breakup of the Farallon plate and initiation of the Cocos–Nazca spreading occurred ∼23 Ma. Assuming a typical mantle flow velocity of ∼8 cm/y as inferred from our numerical simulations (Fig. 3), ∼18 My would be needed for the plume material entrained in the mantle wind to reach the CAM, hence providing a plausible explanation for the emergence of Galápagos plume signatures in the CAM at ∼5 Ma (10) and young volcanism along most of the Cocos Ridge hotspot track, for example Cocos Island (54). While future work is required to constrain the relative roles of the large-scale mantle wind versus channeling along the PFZ, the cross-disciplinary evidence presented in this study argues that the Galápagos plume mantle has been laterally transported at shallow mantle depths over 1,400 km. These results underscore the potential for enriched geochemical anomalies (including high $^3He/^4He$ ratios) to be disseminated away from plume conduits. This mechanism is likely applicable to many plume localities worldwide, whereby high $^3He/^4He$ mantle domains are observed at a distance from the actual plume centers (e.g., ref. 58). Globally, this finding may also explain why high $^3He/^4He$ worldwide is not geographically confined to regions overlying large low shear-wave velocity provinces (e.g., ref. 59), suggesting that the nature and extent of plume–ridge–mantle flow interactions may be key to explaining some of the enriched, plume-like geochemical signatures observed in upper mantle domains far from plumes.

Materials and Methods

Fluid and Gas Sample Collection and Analysis. In 2018, fluid and gas samples were collected across Costa Rica and Panama (Fig. 1), with pH ranging from 3.0 to 10.0 and temperatures in the range 26 to 60 °C. Fluid and gas samples were collected in evacuated glass flasks and copper (Cu) tubes using standard collection procedures (61) whereby precautions were taken to minimize any possible air contamination (62). Gas and fluid samples (n = 25) from 2018 are accompanied by additional (n = 40) samples collected during reconnaissance field campaigns in 2005 (n = 5), 2008 (n = 1), 2010 (n = 11), 2012 (n = 6), 2013 (n = 15), and 2017 (n = 2). He and C isotope data from the initial reconnaissance field campaigns were produced in the Fluids and Volatiles Laboratory at Scripps Institution of Oceanography (SIO), whereas data from 2017 and 2018 are from the University of Oxford (He isotopes), the US Geological Survey Noble Gas Laboratory [He isotopes (63)], and the Tokyo Institute for Technology (C isotopes). Gas and water samples from previous campaigns were analyzed at the SIO for helium and carbon isotopes using instrumentation and protocols described previously (35, 64, 65). All samples were extracted on a dedicated preparation line with a fraction of the noncondensable gas (containing He and Ne) captured in a 1720 glass breakseal. All CO_2 was condensed into a Pyrex breakseal following separation from water vapor, noninert gases (N_2, CO, and CH_4), and heavy noble gases (Ar, Kr, and Xe). Helium and neon analyses were carried out on a MAP-215 noble gas mass spectrometer at the SIO. First, the gas was released from the breakseal and prepared for analysis using a series of active gas getters and traps held at liquid nitrogen temperature. Helium was separated from neon using a helium-cooled refrigeration stage interfaced to a trap lined with activated charcoal. All sample $^3He/^4He$ ratios were normalized to standard aliquots of air processed and analyzed under identical conditions. When considering the reproducibility of He isotope measurements, it is essential to consider the amount of air contamination in a given sample, which is estimated using the relative amount of He and Ne, expressed as the X value [$^4He/^{20}Ne$ normalized to air (27, 66, 67)].

Carbon dioxide was purified at the SIO on a dedicated line using a variable temperature trap designed to separate CO_2 from sulfur-bearing species. Following cleanup, the amount of CO_2 was measured using a capacitance gauge manometer in a calibrated volume before freezing an aliquot of the CO_2 in a Pyrex breakseal. For isotope analysis, the CO_2 aliquot was inlet into a Thermo-Finnigan Delta XPPlus isotope ratio mass spectrometer. Carbon isotopes on gas samples from the 2017 and 2018 campaign were analyzed at the Universidad Nacional on a Picarro G2201-I by acidification of NaOH solutions extracted from Giggenbach bottle samples. $\delta^{13}C_{VPDB}$ values were calibrated against a set of eight standards with values ranging from +2.42 to −37.21‰, including internationally accepted standards NBS19 Limestone and Carrara Marble. Reported $\delta^{13}C$ values have uncertainties of <0.1‰ based on repeat analyses of standards and samples.

Noble gas analysis was also conducted in the Noble Laboratory at the University of Oxford (the 2017 and 2018 samples) using a dual mass spectrometer setup interfaced to a dedicated extraction and purification system (68). Gases were collected in Cu tubes and then transferred to the extraction and purification line where reactive gases were removed by exposing gases to a titanium sponge held at 950 °C. The titanium sponge was cooled for 15 min to room temperature (20 °C) before gases were expanded to a dual hot (SAES GP-50) and cold (SAES NP-10) getter system held at 250 °C and room temperature, respectively. A small aliquot of gases was segregated for preliminary analysis on a Hiden Analytical HAL-200 quadrupole mass spectrometer. All noble gases were then concentrated using a series of cryogenic traps; heavy noble gases (Ar, Kr, and Xe) were frozen down at 15 K on an all stainless steel finger (a stem of the vacuum line), and the He and Ne were frozen down at 19 K on a cold finger filled with charcoal. The temperature on the charcoal finger was then raised to 34 K to release only He, which was inlet into a Helix SFT™ Split Flight Tube Noble Gas mass spectrometer. Following the He analysis, the temperature on the charcoal cryogenic trap was raised to 90 K to release Ne, which was inlet into an ARGUS VI mass spectrometer.

Water samples for carbon isotope analysis (2017 and 2018 samples) of DIC and dissolved organic carbon (DOC) were collected by 50-mL syringes and filtered through a 0.22-μm filter (DISMIC–25AS; Advantec Toyo Kaisha) and directly injected into a prevacuumed 50-mL serum bottle sealed with butyl rubber septa and an aluminum crimp. DIC concentrations and their $\delta^{13}C$ values were measured using CO_2 in the headspace of glass vials after a 1-h reaction with injected 0.5 mL H3PO4. DOC were also measured from CO_2 in the headspace after the reaction of carbonate-free residue with 0.2 g sodium persulfate. The amount of CO_2 and the isotopic values were measured using an Agilent 6890N gas chromatograph attached to a Thermo-Finnigan Delta XPPlus. Two international standards ($\delta^{13}C$ = −13.90 and 2.52‰) were used for standardization, and the SDs were obtained from more than three measurements.

Materials and Methods for the La Providencia Samples. As verified by petrographic studies, samples with no visible weathering were crushed in an alumina jaw crusher and washed with deionized water in an ultrasonic bath.

Alteration-free rock chips (e.g., those free of oxides, veins, and zeolites) were selected under a stereoscopic microscope and powdered in an alumina mill. Homogenous glass disks were produced at Michigan State University by fusing each powdered sample with lithium tetraborate ($Li_2B_4O_7$). The glass disks were then analyzed for major elements and selected trace elements (e.g., Cr, Cu, Ni, Sr, Rb, Zr, and Zn) by X-ray fluorescence in a Bruker S4 Pioneer. Trace elements were obtained in the same glass disks by laser ablation inductively coupled plasma mass spectrometry (ICP-MS) in a Micromass Platform ICP-MS with a Cetac LSX 200+ Nd:YAG laser (266 nm). The details of methods and precision for this laboratory are reported by ref. 69.

Sr-Nd-Pb isotope measurements were carried out on whole rock powders. About 100 mg sample was weighed into a Teflon beaker and then dissolved for 2 d in a 5:1 mixture of HF and HNO_3 at 150 °C. Sample dissolution and element chromatography were carried out at Institut für Meereswissenschaften (IFM)-GEOMAR in Kiel in Class 1000 clean rooms equipped with Class 100 laminar flow hoods. All reagents used were either double distilled in a PicoTrace Teflon distillery (HCl and HNO_3) or certified ultra-pure hydrofluoric acid (HF) and hydrobromic acid (HBr) acids from SEASTAR©. An ELGA© purifying system provided 18.2 MΩ water.

The ion chromatography followed established standard procedures (e.g., ref. 70). These included a two-pass Pb separation and cleanup using 100-μl Teflon microcolumns filled with BIORAD© AG 1 × 8 (100 to 200 mesh) resin that equilibrated with 1 M HBr for highest Pb retention and from which Pb is released with 1 mL 6N HCl. The rest of the sample collected during Pb chromatography was then loaded in 2.5N HCl into 6-mL quartz glass columns filled with BIORAD© AG50W-X8 (100 to 200 mesh) resin to separate Sr. The rare earth elements (REE) were obtained in 6 mL 6N HCl at the final washout of the Sr columns. The REE collection was then loaded in 0.25N HCl and then placed into 4-mL quartz glass columns filled with EICHROM© Ln-Spec resin (100 to 150 μm) to obtain the Nd fraction.

Isotopic ratios were determined by thermal ionization mass spectrometry (TIMS) at IFM-GEOMAR on a TRITON (Sr and Nd) and MAT262 RPQ^{2+} TIMS (Pb). Both instruments operated in static multicollection mode. Sr and Nd isotopic ratios are normalized within each run to $^{86}Sr/^{88}Sr = 0.1194$ and $^{146}Nd/^{144}Nd = 0.7219$, respectively, and all errors are reported as 2 sigma of the mean. The reference material measured along with the samples were normalized and gave $^{87}Sr/^{86}Sr = 0.710250 \pm 0.000008$ ($n = 13$) for NBS 981 and $^{143}Nd/^{144}Nd = 0.511850 \pm 0.000006$ ($n = 8$) for La Jolla. Sr-Nd replicate analyses of sample JK117 were within the external errors of the reference material. The long-term reproducibility of NBS 981 ($n = 197$) is $^{206}Pb/^{204}Pb = 16.899 \pm 0.008$, $^{207}Pb/^{204}Pb = 15.437 \pm 0.009$, and $^{208}Pb/^{204}Pb = 36.525 \pm 0.029$. Pb isotope ratios are normalized to NBS 981 values of ref. 71. Pb replicate analyses of sample JK117 is better than 0.01%/amu. Total chemistry blanks are <50 pg for Sr-Nd and Pb and thus are considered negligible.

Mantle Flow Modeling. To calculate mantle flow, we use the global viscous flow model of ref. 24, which incorporates the effects of 1) plate motions, 2) mantle density structure, and 3) net rotation of the Earth's lithosphere. Plate motions were imposed from the NUVEL-1A model (72) for 13 plates in the no-net-rotation (NNR) reference frame. Mantle density structure was derived by converting seismic velocities anomalies to density anomalies using the S20RTSb seismic tomography model (73) and a constant scaling factor of 0.15 $g \cdot cm^{-3}/km.s^{-1}$ (74). Net rotation of the lithosphere was imposed from the HS3 model (75) but with the magnitude of the rotation scaled by the dimensionless factor (α) ranging from 0 (consistent with NNR) to 1 [consistent with HS3 (75)]. Mantle flow was calculated using the finite element code CitcomS (76, 77) and a grid with 157-km horizontal resolution and vertical resolution varying from 150 km (lower mantle) to 25 km (above 350-km depth). Calculations assume a base viscosity structure that consists of four layers: lithosphere ($1{,}000 \times 10^{21}$ Pa.s), asthenosphere (0.1×10^{21} Pa.s), upper mantle (1.0×10^{21} Pa.s), and lower mantle (50×10^{21} Pa.s), which are scaled by a constant factor (β). The scaling factors $\alpha = 0.2$ and $\beta = 0.5$ were determined by fitting the model to a global dataset of shear-wave splitting data (24).

Data Availability. All study data are included in the article and/or supporting information.

ACKNOWLEDGMENTS. This work was principally supported by Grant G-2016-7206 from the Alfred P. Sloan Foundation and the Deep Carbon Observatory to P.H.B. We also acknowledge the NSF awards (1144559, 1923915, and 2015789) to P.H.B., which partially supported this work. S.Z. was supported by the Australian Research Council Grant DE210100084 and a University of Sydney Robinson Fellowship. D.G. was partially supported by funding from the European Research Council (ERC) under the European Union's Horizon 2020 research and innovation program Grant Agreement No. 948972—COEVOLVE—ERC-2020-STG. This study was also supported in part by NSF award No. EAR 1826673 to E.G. Folkmar Hauff is acknowledged for contributing to the analysis of the La Providencia samples at GEOMAR. We thank Andy Hunt from the US Geological Survey for having performed noble gas measurements on four water samples reported in this study. We also thank Cristian Virrueta and Keith Blackmon for analytical assistance at the SIO. We gratefully thank the two anonymous reviewers and the editor for their thoughtful comments and efforts toward improving our manuscript. We warmly thank the late David Hilton, who pioneered this study and was a mentor and dear friend to many of the coauthors.

1. B. Liu, Y. Liang, The prevalence of kilometer-scale heterogeneity in the source region of MORB upper mantle. *Sci. Adv.* **3**, e1701872 (2017).
2. C. M. Meyzen *et al.*, Isotopic portrayal of the Earth's upper mantle flow field. *Nature* **447**, 1069–1074 (2007).
3. A. Stracke, Earth's heterogeneous mantle: A product of convection-driven interaction between crust and mantle. *Chem. Geol.* **330–331**, 274–299 (2012).
4. C. J. Allègre, D. L. Turcotte, Implications of a two-component marble-cake mantle. *Nature* **323**, 123–127 (1986).
5. A. W. Hofmann, W. M. White, Mantle plumes from ancient oceanic crust. *Earth Planet. Sci. Lett.* **57**, 421–436 (1982).
6. K. E. Donnelly, S. L. Goldstein, C. H. Langmuir, M. Spiegelman, Origin of enriched ocean ridge basalts and implications for mantle dynamics. *Earth Planet. Sci. Lett.* **226**, 347–366 (2004).
7. J. G. Schilling, Upper mantle heterogeneities and dynamics. *Nature* **314**, 62–67 (1985).
8. C. J. Allègre, B. Hamelin, B. Dupré, Statistical analysis of isotopic ratios in MORB: The mantle blob cluster model and the convective regime of the mantle. *Earth Planet. Sci. Lett.* **71**, 71–84 (1984).
9. X. Long *et al.*, Origin of isolated seamounts in the Canary Basin (East Atlantic): The role of plume material in the origin of seamounts not associated with hotspot tracks. *Terra* **32**, 390–398 (2020).
10. E. Gazel *et al.*, Plume-subduction interaction in southern Central America: Mantle upwelling and slab melting. *Lithos* **121**, 117–134 (2011).
11. M. A. Menzies, P. R. Kyle, M. Jones, G. Ingram, Enriched and depleted source components for tholeiitic and alkaline lavas from Zuni-Bandera, New Mexico: Inferences about intraplate processes and stratified lithosphere. *J. Geophys. Res.* **96**, 13645–13671 (1991).
12. N. H. Sleep, Lateral flow of hot plume material ponded at sublithospheric depths. *J. Geophys. Res. B Solid Earth* **101**, 28065–28083 (1996).
13. M. A. Feighner, M. A. Richards, The fluid dynamics of plume-ridge and plume-plate interactions: An experimental investigation. *Earth Planet. Sci. Lett.* **129**, 171–182 (1995).
14. G. Ito, J. Lin, D. Graham, Observational and theoretical studies of the dynamics of mantle plume-mid-ocean ridge interaction. *Rev. Geophys.* **41**, 1017 (2003).
15. Y. Niu, K. D. Collerson, Origin of enriched-type mid-ocean ridge basalt at ridges far from mantle plumes: The East Pacific Rise at 11°20'N. *J. Geophys. Res.* **104**, 7067–7087 (1999).
16. K. A. Kelley, R. Kingsley, J. G. Schilling, Composition of plume-influenced mid-ocean ridge lavas and glasses from the Mid-Atlantic Ridge, East Pacific Rise, Galápagos spreading center, and Gulf of Aden. *Geochem. Geophys. Geosyst.* **14**, 223–242 (2013).
17. T. Mittal, M. A. Richards, Plume-ridge interaction via melt channelization at Galapagos and other near-ridge hotspot provinces. *Geochem. Geophys. Geosyst.* **18**, 1711–1738 (2017).
18. M. Abratis, G. Wörner, Ridge collision, slab-window formation, and the flux of Pacific asthenosphere into the Caribbean realm. *Geology* **29**, 127–130 (2001).
19. M. D. Feigenson, M. J. Carr, S. V. Maharaj, S. Juliano, L. L. Bolge, Lead isotope composition of Central American volcanoes: Influence of the Galapagos plume. *Geochem. Geophys. Geosyst.* **5**, Q06001 (2004).
20. E. R. Benjamin *et al.*, High water contents in basaltic magmas from Irazú Volcano, Costa Rica. *J. Volcanol. Geotherm. Res.* **168**, 68–92 (2007).
21. K. Hoernle *et al.*, Arc-parallel flow in the mantle wedge beneath Costa Rica and Nicaragua. *Nature* **451**, 1094–1097 (2008).
22. S. T. Johnston, D. J. Thorkelson, Cocos-Nazca slab window beneath Central America. *Earth Planet. Sci. Lett.* **146**, 465–474 (1997).
23. Y. Dzierma *et al.*, The steeply subducting edge of the Cocos Ridge: Evidence from receiver functions beneath the northern Talamanca Range, south-central Costa Rica. *Geochem. Geophys. Geosyst.* **12**, Q04S30 (2012).
24. C. P. Conrad, M. D. Behn, Constraints on lithosphere net rotation and asthenospheric viscosity from global mantle flow models and seismic anisotropy. *Geochem. Geophys. Geosyst.* **11**, Q05W05 (2010).
25. D. N. Barfod, C. J. Ballentine, A. N. Halliday, J. G. Fitton, Noble gases in the Cameroon line and the He, Ne, and Ar isotopic compositions of high mu (HIMU) mantle. *J. Geophys. Res.* **104**, 29509–29527 (1999).
26. D. R. Hilton, T. P. Fischer, B. Marty, Noble gases and volatile recycling at subduction zones. *Rev. Mineral. Geochemistry* **47**, 319–370 (2002).
27. P. H. Barry *et al.*, Forearc carbon sink reduces long-term volatile recycling into the mantle. *Nature* **568**, 487–492 (2019).

28. A. Pedroni, K. Hammerschmidt, H. Friedrichsen, He, Ne, Ar, and C isotope systematics of geothermal emanations in the Lesser Antilles islands arc. *Geochim. Cosmochim. Acta* **63**, 515–532 (1999).
29. M. Gasparon, D. R. Hilton, R. Varne, Crustal contamination processes traced by helium isotopes: Examples from the Sunda arc, Indonesia. *Earth Planet. Sci. Lett.* **126**, 15–22 (1994).
30. E. Mason, M. Edmonds, A. V Turchyn, Remobilization of crustal carbon may dominate volcanic arc emissions. *Science* **357** 290–294 (2017).
31. Y. Sano, T. Gamo, S. N. Williams, Secular variations of helium and carbon isotopes at Galeras volcano, Colombia. *J. Volcanol. Geotherm. Res.* **77**, 255–265 (1997).
32. Y. Sano, B. Marty, Origin of carbon in fumarolic gas from island arcs. *Chem. Geol.* **119**, 265–274 (1995).
33. W. G. Mook, J. C. Bommerson, W. H. Staverman, Carbon isotope fractionation between dissolved bicarbonate and gaseous carbon dioxide. *Earth Planet. Sci. Lett.* **22**, 169–176 (1974).
34. Y. Sano, H. Wakita, S. N. Williams, Helium-isotope systematics at Nevado del Ruiz volcano, Colombia: Implications for the volcanic hydrothermal system. *J. Volcanol. Geotherm. Res.* **42**, 41–52 (1990).
35. A. M. Shaw, D. R. Hilton, T. P. Fischer, J. A. Walker, G. E. Alvarado, Contrasting He-C relationships in Nicaragua and Costa Rica: Insights into C cycling through subduction zones. *Earth Planet. Sci. Lett.* **214**, 499–513 (2003).
36. D. R. Hilton *et al.*, Monitoring of temporal and spatial variations in fumarole helium and carbon dioxide characteristics at Poás and Turrialba volcanoes, Costa Rica (2001-2009). *Geochem. J.* **44**, 431–440 (2010).
37. T. P. Fischer *et al.*, Temporal variations in fumarole gas chemistry at Poás volcano, Costa Rica. *J. Volcanol. Geotherm. Res.* **294**, 56–70 (2015).
38. I. MacMillan, P. B. Gans, G. Alvarado, Middle Miocene to present plate tectonic history of the southern Central American Volcanic Arc. *Tectonophysics* **392**, 325–348 (2004).
39. P. J. Hidalgo, T. O. Rooney, Petrogenesis of a voluminous Quaternary adakitic volcano: The case of Baru volcano. *Contrib. Mineral. Petrol.* **168**, 1011 (2014).
40. M. J. Defant *et al.*, The geochemistry of young volcanism throughout western Panama and southeastern Costa Rica: An overview. *J. Geol. Soc. London* **149**, 569–579 (1992).
41. W. M. White, R. A. Duncan, Portrait of a pathological mantle plume I. I Cocos. *J. Geophys. Res.* **98**, 533–563 (1993).
42. K. S. Harpp, W. M. White, Tracing a mantle plume: Isotopic and trace element variations of Galápagos seamounts. *Geochem. Geophys. Geosyst.* **2**, 1042 (2001).
43. K. Hoernle *et al.*, Existence of complex spatial zonation in the Galápagos plume. *Geology* **28**, 435–438 (2000).
44. A. W. Hofmann, K. P. Jochum, M. Seufert, W. M. White, Nb and Pb in oceanic basalts: New constraints on mantle evolution. *Earth Planet. Sci. Lett.* **79**, 33–45 (1986).
45. J. Hermann, D. Rubatto, Accessory phase control on the trace element signature of sediment melts in subduction zones. *Chem. Geol.* **265**, 512–526 (2009).
46. L. B. Carter, S. Skora, J. D. Blundy, J. C. M. De Hoog, T. Elliott, An experimental study of trace element fluxes from subducted oceanic crust. *J. Petrol.* **56**, 1585–1606 (2014).
47. E. Gazel *et al.*, Long-lived source heterogeneities in the Galapagos mantle plume. *Geochem. Geophys. Geosyst.* **19**, 2764–2779 (2018).
48. M. D. Kurz, S. K. Rowland, J. Curtice, A. E. Saal, T. Naumann, "Eruption rates for Fernandina Volcano: A new chronology at the Galápagos Hotspot Center" in *The Galapagos: A Natural Laboratory for the Earth Sciences*, K. S. Harpp, E. Mittelstaedt, N. dà'Ozouville, D. W. Graham, Eds. (*Geophysical Monograph Series*, John Wiley & Sons, Washington, DC, 2014), pp. 41–54.
49. Y. W. Chen, L. Colli, D. E. Bird, J. Wu, H. Zhu, Caribbean plate tilted and actively dragged eastwards by low-viscosity asthenospheric flow. *Nat. Commun.* **12**, 1603 (2021).
50. N. H. Sleep, Channeling at the base of the lithosphere during the lateral flow of plume material beneath flow line hot spots. *Geochem. Geophys. Geosyst.* **9**, Q08005 (2008).
51. S. A. Gibson, M. A. Richards, Delivery of deep-sourced, volatile-rich plume material to the global ridge system. *Earth Planet. Sci. Lett.* **499**, 205–218 (2018).
52. D. R. Villagómez, D. R. Toomey, D. J. Geist, E. E. E. Hooft, S. C. Solomon, Mantle flow and multistage melting beneath the Galápagos hotspot revealed by seismic imaging. *Nat. Geosci.* **7**, 151–156 (2014).
53. D. W. Graham *et al.*, "Helium isotope variations and mantle plume-spreading ridge interactions along the Galápagos Spreading Center" in *The Galapagos: A Natural Laboratory for the Earth Sciences*, K. S. Harpp, E. Mittelstaedt, N. dà'Ozouville, D. W. Graham, Eds. (*Geophysical Monograph Series*, John Wiley & Sons, Washington, DC, 2014), pp. 393–414.
54. J. M. O'Connor, P. Stoffers, J. R. Wijbrans, T. J. Worthington, Migration of widespread long-lived volcanism across the Galápagos Volcanic Province: Evidence for a broad hotspot melting anomaly? *Earth Planet. Sci. Lett.* **263**, 339–354 (2007).
55. R. Werner, K. Hoernle, U. Barckhausen, F. Hauff, Geodynamic evolution of the Galápagos hot spot system (Central East Pacific) over the past 20 m.y.: Constraints from morphology, geochemistry, and magnetic anomalies. *Geochem. Geophys. Geosyst.* **4**, 1108 (2003).
56. V. Levin, S. Elkington, J. Bourke, I. Arroyo, L. Linkimer, Seismic anisotropy in southern Costa Rica confirms upper mantle flow from the Pacific to the Caribbean. *Geology* **49**, 8–12 (2021).
57. R. M. Russo, P. G. Silver, Trench-parallel flow beneath the Nazca plate from seismic anisotropy. *Science (80-.)* **263**, 1105–1111 (1994).
58. S. Harðardóttir, S. A. Halldórsson, D. R. Hilton, Spatial distribution of helium isotopes in Icelandic geothermal fluids and volcanic materials with implications for location, upwelling and evolution of the Icelandic mantle plume. *Chem. Geol.* **480**, 12–27 (2018).
59. M. G. Jackson, T. W. Becker, B. Steinberger, Spatial characteristics of recycled and primordial reservoirs in the deep mantle. *Geochem. Geophys. Geosyst.* **22**, e09525 (2021).
60. G. Zandt, E. Humphreys, Toroidal mantle flow through the western U.S. slab window. *Geology* **36**, 295–298 (2008).
61. W. F. Giggenbach, R. L. Goguel, "Collection and analysis of hydrothermal and volcanic water and gas discharges" (Rep. No. CD 2401, Chem. Div. DSIR, Petone, New Zealand, 1989).
62. P. H. Barry *et al.*, Helium and carbon isotope systematics of cold "mazuku" CO2 vents and hydrothermal gases and fluids from Rungwe Volcanic Province, southern Tanzania. *Chem. Geol.* **339**, 141–156 (2013).
63. A. G. Hunt, U. S. Geological Survey Noble Gas Laboratory's standard operating procedures for the measurement of dissolved gas in water samples. *U.S. Geol. Surv. Tech. Meth.* **5**, 1–22 (2015).
64. G. A. M. de Leeuw, D. R. Hilton, T. P. Fischer, J. A. Walker, The He–CO2 isotope and relative abundance characteristics of geothermal fluids in El Salvador and Honduras: New constraints on volatile mass balance of the Central American Volcanic Arc. *Earth Planet. Sci. Lett.* **258**, 132–146 (2007).
65. J. T. Kulongoski, D. R. Hilton, A quadrupole-based mass spectrometric system for the determination of noble gas abundances in fluids. *Geochem. Geophys. Geosyst.* **3**, 1–10 (2002).
66. C. J. Ballentine, R. Burgess, B. Marty, Tracing fluid origin, transport and interaction in the crust. *Rev. Mineral. Geochemistry* **47**, 539–614 (2002).
67. P. H. Barry *et al.*, Helium, inorganic and organic carbon isotopes of fluids and gases across the Costa Rica convergent margin. *Sci. Data* **6**, 284 (2019).
68. P. H. Barry *et al.*, Noble gases solubility models of hydrocarbon charge mechanism in the Sleipner Vest gas field. *Geochim. Cosmochim. Acta* **194**, 291–309 (2016).
69. R. S. Hannah *et al.*, Origin of silicic volcanic rocks in Central Costa Rica: A study of a chemically variable ash-flow sheet in the Tiribí Tuff. *Bull. Volcanol.* **64**, 117–133 (2002).
70. S. E. Hart, C. Brooks, Clinopyroxene-matrix partitioning of K, Rb, Cs, Sr and Ba. *Geochim. Cosmochim. Acta* **38**, 1799–1806 (1974).
71. S. J. G. Galer, W. Abouchami, Practical application of lead triple spiking for correction of instrumental mass discrimination. *Mineral. Mag. A* **62A**, 491–492 (1998).
72. C. DeMets, R. G. Gordon, D. F. Argus, S. Stein, Effect of recent revisions to the geomagnetic reversal time scale on estimates of current plate motions. *Geophys. Res. Lett.* **21**, 2191–2194 (1994).
73. J. Ritsema, W. Xu, L. Stixrude, C. Lithgow-Bertelloni, Estimates of the transition zone temperature in a mechanically mixed upper mantle. *Earth Planet. Sci. Lett.* **277**, 244–252 (2009).
74. S. Karato, B. B. Karki, Origin of lateral variation of seismic wave velocities and density in the deep mantle. *J. Geophys. Res.* **106**, 21771–21783 (2001).
75. A. E. Gripp, R. G. Gordon, Young tracks of hotspots and current plate velocities. *Geophys. J. Int.* **150**, 321–361 (2002).
76. S. Zhong, M. T. Zuber, L. Moresi, M. Gurnis, The role of temperature-dependent viscosity and surface plates in spherical shell models of mantle convection. *J. Geophys. Res. Atmos.* **105**, 11063–11082 (2000).
77. E. Tan, E. Choi, P. Thoutireddy, M. Gurnis, M. Aivazis, GeoFramework: Coupling multiple models of mantle convection within a computational framework. *Geochem. Geophys. Geosyst.* **7**, 1–14 (2006).